FINAL TECHNICAL PROGRESS REPORT

Award Number: DE-SC0010610

Program Manager: Dr. Viviane Schwartz, Catalysis Science Program, Office of Basic Energy Sciences

Recipient Institution: University of Massachusetts, Amherst

Project Title: Computational Design of Graphene–Nanoparticle Catalysts

Principal Investigator: Dr. Ashwin Ramasubramaniam, Associate Professor
University of Massachusetts Amherst
160 Governors Drive, Amherst MA 01003
E-mail: ashwin@engin.umass.edu
Phone: (413) 545-4866

Report Date: November 23, 2019

Period Covered: September 1, 2013 – August 31, 2019

This is the final technical report for this 5-year research project (with a 1-year no-cost extension).

ABSTRACT

Nanoclusters possess electronic properties that are inherently different from their bulk counterparts due to quantum effects that are strongly manifested at the nanoscale. Therefore, the catalytic properties of nanoclusters cannot be understood by a simple extrapolation of our understanding of catalysis on bulk metal surfaces. The presence of supports further modifies the electronic properties, morphology, and catalytic activity of a nanoparticle due to interplay between the electronic properties of the support and the nanoparticle. The objective of this research was to develop a systematic computational approach for designing and evaluating the activity and selectivity of supported catalyst nanoclusters, in the specific context of graphene-supported Pt and Pt-Ru nanoparticles for methanol decomposition. While the enhanced activity of nanoclusters has long been exploited in Pt–carbon black catalysts, recent experiments have shown that Pt–graphene catalysts can far outperform their predecessors, in particular, for methanol oxidation—a reaction of crucial importance for methanol fuel cells. However, the fundamental mechanisms by which graphene enhances the activity of nanoparticles for methanol oxidation as yet remain to be understood.

Over the course of this research, we developed a comprehensive computational program toward modeling and understanding the activity of Pt nanoparticles on graphene supports. We developed genetic algorithms to identify low-energy isomers of Pt clusters on both pristine and defective (experimentally realistic) graphene supports. From structure devolve other properties such as reactivity and selectivity, which were probed in the context of CO oxidation and methanol decomposition. Motivated by the need for accurate structure prediction, we developed a new tight-binding parameterization for Pt-Ru alloys as well as empirical potential parameters for the Pt-Ru-C system to model support–cluster interactions. In conjunction with genetic algorithms, these tight-binding/empirical potential parameters allowed for efficient prediction of low energy structures that were then analyzed in greater detail with density functional theory (DFT). In particular, DFT modeling shows that strong cluster–support interactions—especially at point defects in graphene supports—are beneficial in rendering the Pt nanoclusters more tolerant to CO poisoning. Via DFT-informed microkinetic modeling, defective graphene-supported graphene Pt clusters were shown to be as active as Pt(111) surfaces for methanol decomposition further confirming that Pt-graphene nanocomposites can indeed efficiently catalyze this reaction with significantly lower Pt loading than traditional Pt catalysts. Interestingly, the active pathways on nanoclusters were altered relative to the bulk (111) surface indicating the potential for control over reaction intermediates, mediated by a combination of electronic and structural features of supported clusters. For Pt-Ru alloy clusters, our DFT-informed genetic algorithms consistently predict the formation of low-energy Ru-core/Pt-shell nanoparticles, thereby maximizing the use of expensive Pt for catalyzing surface reactions. Our studies open new avenues for computationally guided design of supported nanoclusters catalysts and, specifically, provide a sound theoretical basis for rational design of nanoparticle–graphene composites for fuel cell electrodes.

DESCRIPTION OF RESEACH ACCOMPLISHMENTS

1. CO Adsorption on Graphene-Supported Pt Nanoclusters

We systematically investigated, via density functional theory (DFT) calculations, the binding of CO to catalytically active Pt nanoclusters. CO is a well-known catalyst poison and also the thermodynamic sink in several energy conversion pathways of interest to us such as methanol or formic acid decomposition. Efficient removal of CO by oxidation is thus critical for ensuring sustained catalytic performance. Graphene–supported Pt nanoclusters have been shown in experiments to possess improved tolerance towards CO poisoning although the precise mechanism that leads to this effect is not understood. We made significant progress in unraveling, at the electronic structure level, the cause of this improved tolerance and establishing the key role of cluster–substrate interactions. [1]

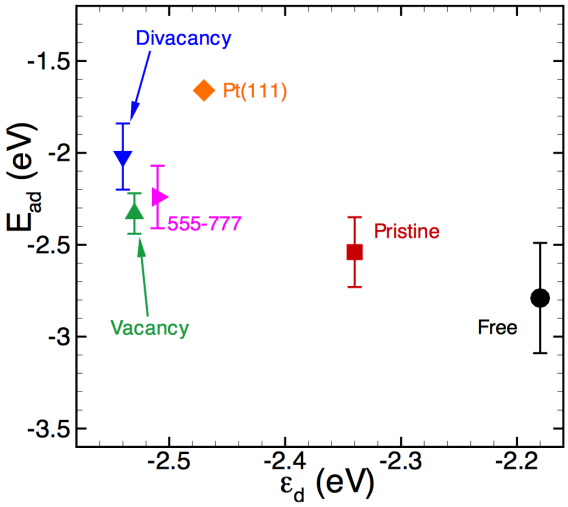

Figure 1: CO adsorption energy (E_{ad}) as a function of *d*-band center (ε_d) relative to the Fermi energy for supported Pt_{13} clusters, free Pt_{13} clusters, and Pt(111) surface. A downshift of the cluster *d*-band center with respect to the Fermi level (more negative ε_d) is directly correlated with weaker adsorption of CO on the cluster. Error bars indicate 95% confidence intervals obtained from sampling over multiple adsorption sites on the cluster.

In previous work, we established that defects in graphene substrates act as strong binding sites for Pt nanoclusters through the formation of strong Pt-C bonds. In addition to stabilizing clusters against sintering, the formation of these strong Pt-C bonds causes a downshift in the average position of the cluster *d*-band, which is then expected to lead to weaker adsorption of molecules on the cluster. [2] In this project, we explicitly investigated CO binding on unsupported and graphene-supported clusters. In general, the adsorption energy of CO to a binding site depends sensitively upon the coordination of cluster the atom(s) at the binding site. For Pt nanoclusters, which typically display several near-degenerate isomers, this variability in local coordination results in variations in CO binding energy of ~0.2 eV, an order of magnitude smaller than the binding energy. [1] To a good approximation then, variability in coordination of cluster atoms can be averaged out by statistical sampling over several configurations of adsorbed CO molecules. The remaining differences in CO binding energies can then be attributed to cluster–substrate interactions and systematically analyzed. Figure 1 displays the average adsorption energy of CO on unsupported and supported Pt_{13} clusters as a function of the cluster *d*-band center, which in turn is affected by the strength of binding between the cluster and the graphene support. For defective support, the cluster–support binding is much stronger leading to a downshift of the *d*-band center relative to the Fermi level. This in turn leads to weaker adsorption of CO on the cluster and provides one possibility for employing defect engineering of substrates as a means of controlling cluster catalytic activity. Similar results were obtained for oxygen binding as well.

Given that CO binding to Pt_{13} clusters is substantially stronger (by 0.7-0.8 eV) than O, the Pt cluster is expected to be *fully saturated* by CO under normal operating conditions. Therefore, we went beyond single-CO adsorption studies and systematically saturated and optimized Pt_{13} clusters with DFT. An interesting and unexpected outcome of studies of CO saturation of Pt_{13} clusters is shown in Figure 2. As seen, for a cluster supported on pristine graphene, CO can intercalate between the support and the cluster, bind to the cluster, and cause complete desorption of the cluster from the support, leading to catalyst loss. Such cluster desorption does not occur when a cluster is bound to a support defect though—which we confirmed more thoroughly with high-temperature *ab* initio MD simulations—further emphasizing the role of support defects in stabilizing catalyst clusters.

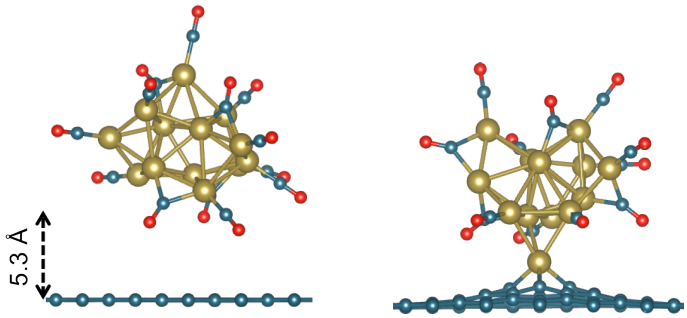

Figure 2: (Left) Spontaneous desorption of a Pt_{13} cluster from a pristine graphene support upon saturation with CO. (Right) CO-saturated Pt_{13} cluster bound to a vacancy in the graphene support.

This work was published in the Journal of Physical Chemistry C. [1, 3]

2. CO Oxidation on Graphene-Supported Pt Nanoclusters

While the weaker adsorption energy of CO on defective-graphene-supported Pt nanoclusters provides a possible explanation for improved CO tolerance of Pt-graphene nanocomposites, it does not furnish proof (other than through indirect Bronsted-Evans-Polyani arguments) of a reduced reaction barrier for CO oxidation. To conclusively establish this, we performed systematic DFT calculations of CO oxidation on supported and unsupported Pt_{13} nanoclusters. [3] In general, CO adsorption energies and oxidation barriers depend sensitively upon the coordination of catalyst atom(s) at the binding site. Unlike crystalline facets, the local coordination on a nanocluster is highly variable and requires expensive DFT-based statistical sampling. Site-to-site variations in adsorption energies and reaction barriers are nevertheless sufficiently small such that signatures of cluster–substrate interactions can still be identified and systematically analyzed.

As noted above, since CO* binding to Pt_{13} clusters is substantially stronger (by 0.7-0.8 eV) than O*, the Pt cluster is expected to be *fully saturated* by CO under normal operating conditions. Therefore, in departure from most studies in the literature, we went beyond single-CO oxidation studies and studied CO oxidation on fully saturated clusters. We examined reaction pathways that proceed via CO*-assisted O_2 activation without the involvement of adsorbed O_2* precursors, which is known to be favored over the Langmuir-Hinshelwood mechanism. Using the Climbing Nudged Elastic Band Method, we sampled multiple reaction sites and trajectories on supported as well as unsupported Pt_{13} clusters, examples of which are displayed in Figure 3. The reaction initiates via CO*-assisted O_2 activation in the vicinity of the CO-covered Pt_{13} cluster and proceeds with the formation of an O*–O–C*–O complex, which subsequently decomposes to CO_2 and an adsorbed O* species. The mechanism is similar to that proposed by Neurock, Iglesia, and coworkers for CO oxidation at an unsupported cuboctahedral Pt_{201} cluster: neither the involvement of adsorbed O_2* precursors nor O_2 dissociation are

necessary; instead, there is direct reaction of O_2 with pre-adsorbed CO* on the cluster. Typically, the O*–O–C*–O complex dissociates exothermically to CO_2 and O*. The support effect in these reactions is appreciable: CO oxidation on unsupported Pt_{13} clusters requires significantly higher activation energies (~1.22-1.97 eV) as compared to CO-covered Pt_{13} clusters bound at point defects in graphene (~0.3-0.9 eV). The fundamental cause of this large difference in energy barriers can be attributed to the downshift of the *d*-levels for clusters bound at graphene point defects. The normally strong CO binding is then weakened and, in keeping with the Sabatier principle, the barrier for CO oxidation is lowered. Defective-graphene-supported Pt_{13} nanoclusters are thus identified as effective catalysts for CO reduction with significantly lower activation energies than unsupported clusters. In the course of our studies, we also identified an oxidation pathway (hitherto only reported on Au) wherein, after the CO*-assisted O_2 activation, the system falls into a stable minimum forming a carbonate-like CO_3* intermediate, which then endothermically dissociates into O* and CO_2. The apparent activation energy for this pathway is typically higher than the exothermic pathway discussed above though, and is expected to be less kinetically relevant.

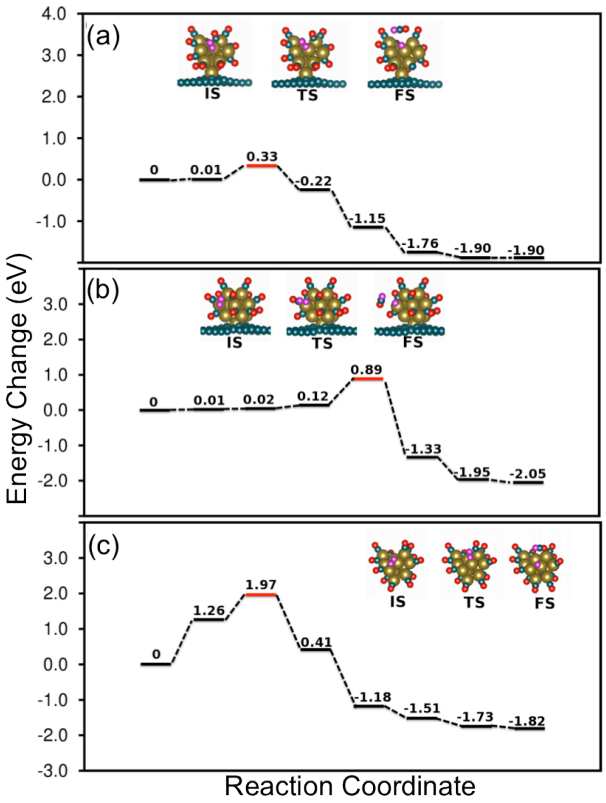

Figure 3: Sample energy profiles for CO oxidation on Pt_{13} clusters (a) at a vacancy on graphene, (b) at a divacancy on graphene, and (c) without a support.

This work was published in the Journal of Physical Chemistry C. [3]

3. Development of Genetic Algorithms for Structural Optimization of Supported Clusters

We implemented and comprehensively tested a Genetic Algorithm (GA) to enable calculation of low-energy structures of supported nanoclusters. [4] Our GA implementation interfaces directly with the widely used, open-source LAMMPS simulation package, which supports a wide range of interatomic potentials, thus allows for facile porting of the GA to different materials.

We have already shown in previous work [2] that Pt_{13} nanoclusters do not adopt high-symmetry morphologies, as commonly assumed. Our GA now provides a robust approach for calculating ground-state morphologies of nanoclusters (10-100 atoms being the range of interest) using empirical potentials for initial screening; this initial step substantially reduces the subsequent computational effort for DFT analysis of candidate low-energy structures.

Figure 4 displays a collection of selected results from our studies. We first characterized Pt clusters in vacuum to benchmark our GA against results from the literature. As seen in Figure 4(a), minimum energy Pt clusters are essentially 2D up to a size of eight atoms beyond which they adopt a 3D structure. This is also found to be the case on pristine (defect-free) graphene supports. The presence of support defects, however, results in clusters being 3D at all sizes. Focusing on Pt_{13} clusters as a particular case, we see from Figure 4(b) that cluster morphology is closely related to energetics. There is a near-continuum of low-energy isomers and, within a window of 1-2 eV of the lowest energy state, one sees a clear correlation between cluster size, as quantified by the radius of gyration, and the total energy: compact clusters are energetically preferred. We also carried out more careful DFT studies of several low-energy isomers of both unsupported and supported Pt_{13} clusters. First, as seen from the upper panel of Figure 4(c), for unsupported clusters within a window of ~0.2 eV in formation energies, there is a small but clear linear variation in the *d*-band center over a range of ~0.1 eV. For supported clusters, the adsorption energy on the support is found to be a better metric that correlates with the *d*-band center. In agreement with our previous work (but with more extensive sampling here), [1, 2] we find that both the charge transferred to the support as well as the *d*-band center are directly correlated with the strength of cluster–support binding. Interestingly, the precise nature of the support point defect (vacancy/divacancy) is less important; the binding strength of the cluster to the support is the primary predictor of the charge transfer and the *d*-band shifts.

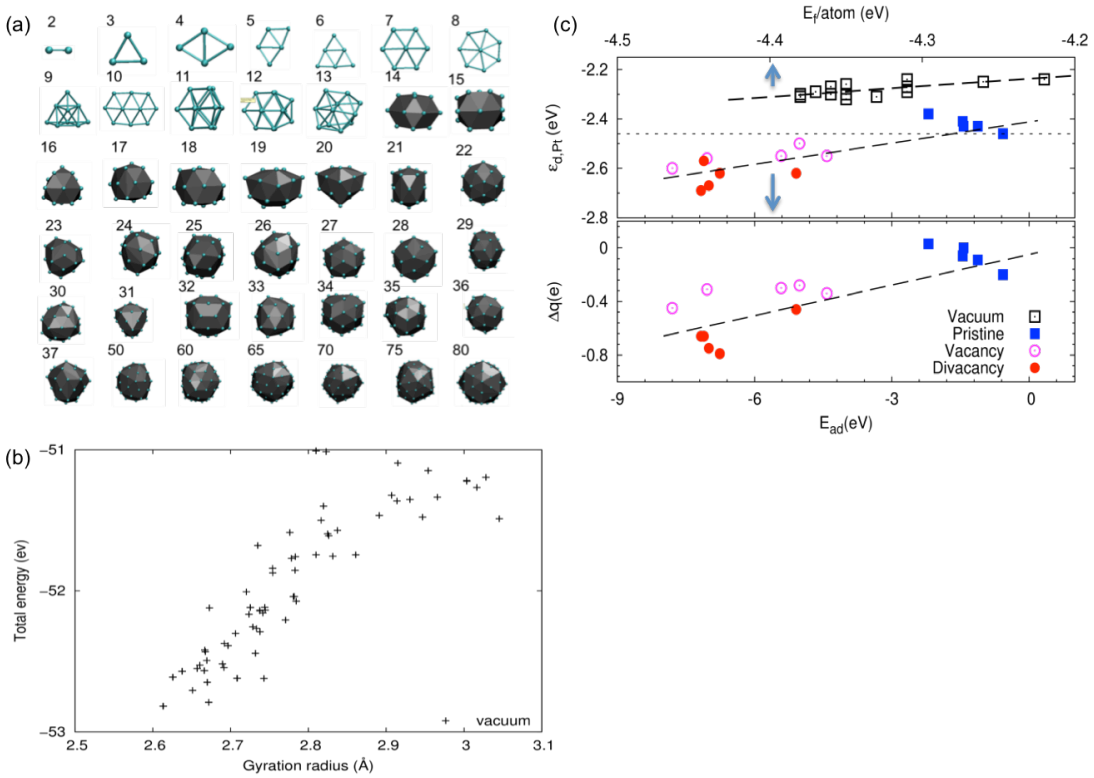

Figure 4: (a) Minimum energy structures for Pt clusters in vacuum from Tersoff-Brenner potential-based GA calculations. (b) Total energy of Pt_{13} clusters versus the radius of gyration (R_g) as obtained from GA calculations. A smaller value of R_g results in a more compact cluster, which is energetically more preferable. (c) Positions of *d*-band centers (upper panel) and charge transfer from Pt_{13} clusters to support (lower panel) relative to adsorption energies on pristine and defective graphene supports. Also shown are *d*-band positions for several low-lying isomers of Pt_{13} clusters in vacuum as a function of their formation energy.

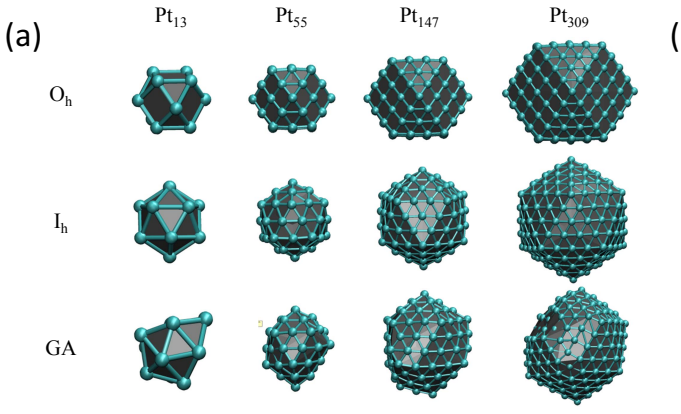

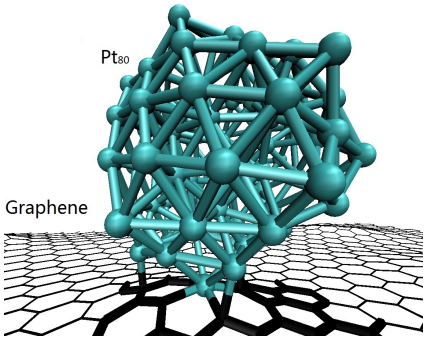

	Pt_{13}		Pt_{55}		Pt_{147}		Pt_{309}	
	DFT	EP	DFT	EP	DFT	EP	DFT	EP
I_h	1.3	1.7	5.1	6.4	6.5	5.1	7.7	5.6
O_h	2.0	1.8	3.3	3.4	8.2	12.4	9.7	18.4
GA	0.0	0.0	0.0	0.0	0.0	0.0	0.0	0.0

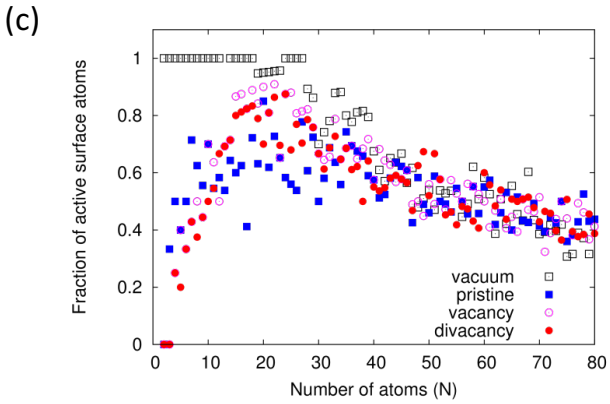

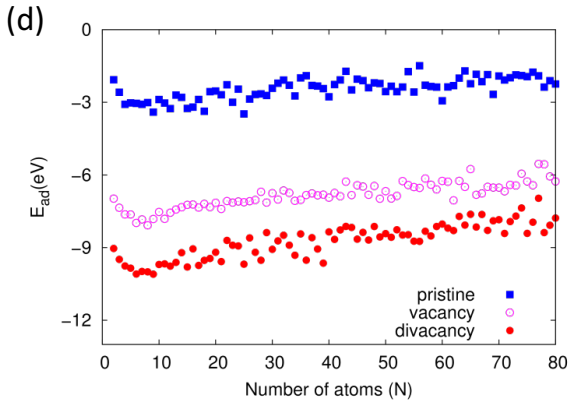

Figure 5: (a) Comparison of select "magic-number" clusters considering both high-symmetry (icosahedral - I_h and cuboctahedral - O_h) and GA-optimized structures. The table lists energy differences (in eV) calculated either with the empirical potential (EP) or DFT, relative to the lowest energy structure, which in all cases is manifestly *not* a high-symmetry morphology. (b) Example of a Pt_{81} cluster bound at a vacancy defect in graphene obtained from GA-optimization. (c) Fraction of active surface atoms from comprehensive characterization of unsupported and supported Pt clusters. For all supported clusters, the maximum fraction of surface-active sites is obtained in the size range of 20-30 atom clusters. (d) Adsorption energies (E_{ad}) of GA-optimized clusters on defect-free and defective graphene supports as a function of cluster size (more negative energies indicate stronger binding). While binding becomes slightly weaker with increasing cluster size, binding to point defects is substantial for all sizes sampled here, indicating the ability of point defects to inhibit catalyst sintering.

Beyond studies of unsupported clusters, our GA now enables significant advances in modeling of *supported clusters*, an example being displayed in Figure 5(b). Starting from a support—here, graphene with or without point defects—and random initial Pt cluster morphology, the GA produces an optimized, low-energy structure of the supported cluster. It is worth noting that there are no *a priori* modeling assumptions here beyond the nature of the support defect; wetting interactions between the cluster and the support, and consequent implications for cluster morphology, are governed fully by the potential energy surface for the composite system. We have exhaustively characterized such supported clusters focusing on catalytically relevant properties such as cluster–support charge transfer, cluster *d*-band shifts, binding energies to point defects, 2D to 3D shape transitions, etc., as well as correlations

between such properties with the aim of identifying simple descriptors. A particularly interesting structural property of supported Pt clusters is highlighted in Figure. 5(c), which shows that clusters in the size range of 20-30 atoms provide the highest fraction of active surface sites. *This new prediction now provides a design target for optimal utilization of precious Pt metal for carbon-supported heterogeneous catalysts*. Interestingly, these cluster sizes are also within the window where support defects can exert a beneficial effect on reaction kinetics while simultaneously stabilizing clusters against catalyst sintering [Figure. 5(d)].

We applied this combined empirical-potential-based GA optimization and DFT electronic structure prediction in several follow-on works—machine learning, Pt-Ru alloy nanoclusters, and methanol decomposition on Pt—reported below

This work was published in the Journal of Physical Chemistry C. [4]

4. Machine-Learning Algorithms Applied to CO Binding on Pt Nanoclusters

Platinum nanoparticles are extensively used as catalysts for electrochemical reactions. While it is generally desirable to minimize the size of nanoparticles to attain high electrocatalytic surface area while optimally utilizing the precious metal, ultra-small (~1 nm) nanoparticles begin to present significant deviations in properties relative to their larger, bulk-like counterparts. From the standpoint of catalyst design, it then becomes imperative to seek appropriate descriptors that can provide insight into the *local* as well as *global* (average) behavior of the surface active sites. We have pursued this challenging problem in the context of CO adsorption on Pt nanoclusters.

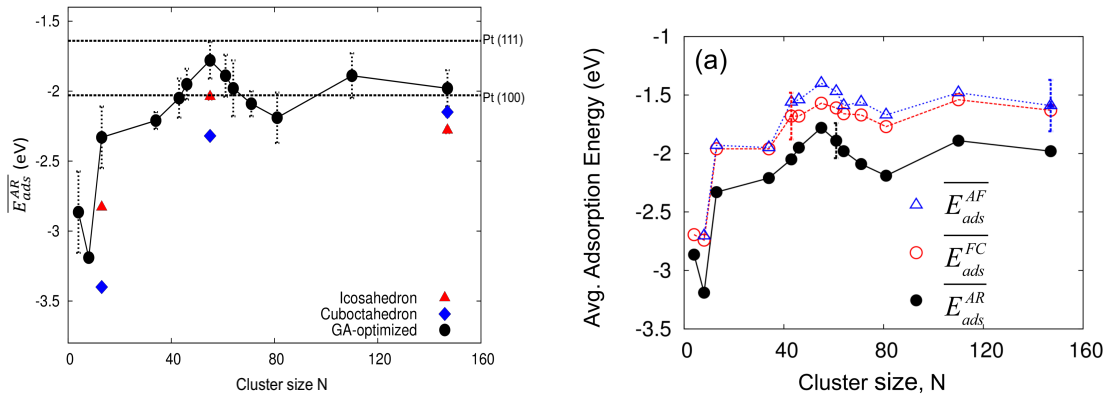

Figure 6: (Left) Average adsorption energy of a single CO molecule as a function of cluster size on lower-energy, low-symmetry, GA-optimized Pt clusters found, and on high-symmetry icosahedral and cuboctahedral clusters. Horizontal dashed lines indicate the reference adsorption energy values on bulk-terminated, FCC Pt(111) and (100) surfaces. (Right) Average single-molecule CO adsorption energies on Pt clusters calculated with a fully frozen configuration (AF), relaxed CO but frozen Pt clusters (FC), and fully relaxed configurations (AR).

As ultra-small nanoclusters have no well-defined surface structure (e.g., facets, edges, corners) each surface site is, in principle, distinct from the point of catalytic activity. Thus, the first key feature of our work—at variance with previous studies—is that we conducted CO adsorption calculations on low-symmetry, low-energy nanoclusters. These cluster morphologies were obtained by the application of an empirical bond-order potential driven GA, developed in our previous work. [4] This approach allows us to examine realistic minimum-energy structures for any given size of nanoparticle and, moreover, eliminates having to decide between the fitness

of various arbitrary, high-symmetry geometries. Once low-energy cluster morphologies are obtained from the GA at relatively low computational cost, the remainder of the computational effort is expended in higher-level DFT calculations of adsorbate binding on these clusters. One of the main challenges of investigating adsorbate binding on these low-symmetry structures is that they generally do not possess symmetry-equivalent sites unlike bulk-terminated crystal facets and high-symmetry clusters. Because of this, some form of statistical sampling must be undertaken for calculating even simple adsorption properties, requiring a compromise between accuracy and computational effort spent on repeatedly sampling the same cluster. Thus, it becomes extremely useful to be able to predict both average as well as site-specific adsorption energies on these disordered structures using relatively simple structural metrics and/or limited electronic structure information without having to undertake full-blown DFT adsorption calculations on every available surface site. In order to approach this challenge, the second key feature of our work is the application of machine learning algorithms—a topic of increasing interest in materials science—to the prediction of CO adsorption energies on sub-nanometer Pt clusters.

We studied Pt nanoclusters, ranging from 0.2–1.5 nm in diameter, to understand size-dependent trends in the energetics of CO binding, and to correlate these with morphological and

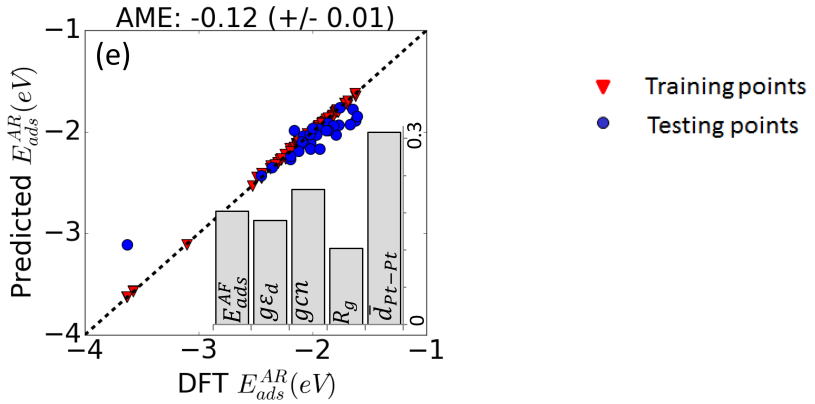

Figure 7: DFT-calculated CO adsorption energies on the surface sites of Pt clusters versus the prediction from machine-learning model. Reported AME (absolute mean error) of the model predictions are the average over five-fold cross validation to avoiding splitting bias. The displayed data points are from one such randomly split dataset. Inset shows the relative importance of the descriptors in the models.

electronic descriptors. As seen from Figure 6, GA-optimized clusters show a non-monotonic trend of surface *d*-band centers with respect to size, going from very high values at small sizes to a minimum around Pt_{100}, before slowly asymptoting towards the Pt(111) surface value. This is in clear contrast to the essentially monotonic behavior of high-symmetry, cuboctahedral and icosahedral morphologies, which are not true low-energy structures for sub-nanometer Pt clusters. The CO adsorption behavior on GA-optimized clusters (Fig. 3) also presents similar non-monotonic behavior with a global maximum at around Pt_{55}. It is therefore clear that traditional single descriptor models based on *d*-band center energies or coordination number, which work well for crystal surfaces, are not suited to nanoclusters; this was also confirmed rigorously through statistical methods. By applying machine-learning algorithms to this large dataset, we were able to establish multi-descriptor models based on *d*-band centers, structural information (coordination number, bond lengths, cluster size), and the "all-frozen" adsorption

energy (a new descriptor that we proposed) that quantitatively predict CO adsorption energies across the whole range of cluster sizes and binding environments (Figure 7). The success of our approach now suggests a route for calculating system descriptors, at minimal computational overhead, which can be applied broadly across other systems to predict site-specific adsorption energies with higher accuracy.

This work was published in the Journal of Physical Chemistry C. [5]

5. Density-Functional Tight-Binding Approach for PtRu alloys

Platinum and platinum-group metals are widely used as electrocatalysts in hydrogen-based or methanol-based proton-exchange-membrane fuel cells (PEMFCs). Pt-Ru alloys, in particular, are among the best oxidation electrocatalysts, displaying high activity, resistance to CO poisoning, and longevity. The superior performance of PtRu over Pt clusters has been explained by invoking the ligand effect, which reduces the binding strength of CO at active sites, as well as a bifunctional mechanism, which accesses alternate pathways of reduced energy barriers for the oxidation and elimination of CO. Yet, there remain important gaps in our systematic understanding of the influence of size, structure, and composition of PtRu alloys on catalytic performance at the nanoscale (alloy nanoclusters).

A significant bottleneck in modeling alloy nanoclusters is the ability to obtain correct ground-state morphologies that can then be systematically studied for catalytic activity. While density-functional theory (DFT) remains the workhorse for modeling reaction thermodynamics and kinetics, it is still too expensive to use within global minimization approaches. Density-functional tight-binding (DFTB) represents a powerful alternative that has been widely employed for studying carbon-based systems and metals with delocalized valance electrons. The computational speed of DFTB is intermediate between accurate but expensive DFT and inexpensive but less-accurate empirical potential methods thereby opening up possibilities for global optimization for larger clusters sizes with high accuracy. *Our new DFTB parameter set is the first such set for Pt, Ru, and PtRu alloys, providing the community with a powerful modeling tool for studying this technologically important alloy system.* [6]

To develop our new DFTB First, we performed DFT calculations on randomly generated PtRu clusters of varying size (13-81 atoms) and composition to create a large database (approximately 200 samples) of equilibrium (structurally optimized) and non-equilibrium (artificially deformed) structures, energies, and forces. Thereafter, 50% of this database was used as a training set to parameterize DFTB potentials for Pt-Pt, Pt-Ru and Ru-Ru interactions; the remaining 50% of the database was used as a testing set to ascertain the accuracy of the DFTB-predicted energetics relative to DFT (Figure 8). Since the clusters used in the fitting procedure were randomly generated, the ability of the DFTB potentials to predict minimum energy configurations of clusters with accuracy remained to be verified. Therefore, as the second phase of the simulations, the potential energy surface generated by the Pt-Ru DFTB model was sampled using a Genetic Algorithm (GA) and minimum energy configurations calculated for a selected set of clusters of varying sizes and compositions (see Figure 9). *The GA code was implemented in-house and was MPI-parallelized for scalability*. The DFTB-optimized minimum energy clusters were imported into VASP and further minimized using a conjugate-gradient algorithm (local minimization) at the DFT level. The DFTB and DFT results were then

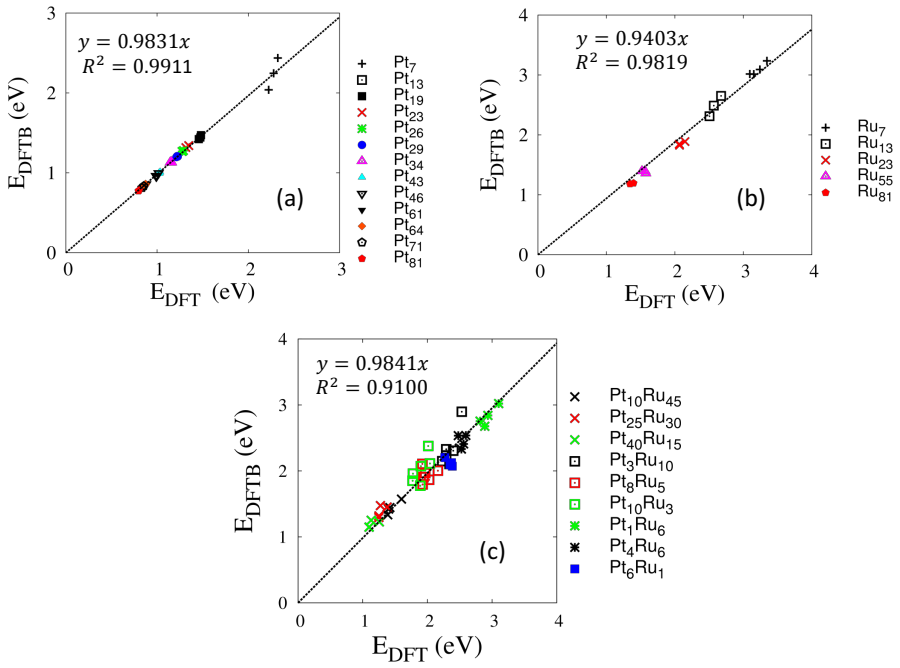

Figure 8: Comparison of DFT and DFTB formation energies of Pt, Ru and PtRu clusters. Dashed lines indicate the least-squares fit to the data. The slopes of the lines (ideally unity) and the R^2 values indicate an accurate DFTB representation of the target DFT data.

compared in terms of cluster formation energies to validate trends across cluster sizes and compositions. As seen from Figure 9, the clusters exhibit low-symmetry morphologies in all cases with little or no resemblance to high-symmetry icosahedral or cuboctahedral geometries as is often assumed *ad hoc* in computational studies. In particular, the finding that low-energy Pt clusters typically adopt low-symmetry structures at small sizes is consistent with several prior studies confirming the validity of our new DFTB potentials. In the case of PtRu alloy clusters, it is well known from several experimental studies that Pt atoms preferentially occupy surface sites whereas Ru atoms segregate towards the core sites. This is also borne out by our simulations, as seen from Figure 9, wherein we consistently find segregation of Pt atoms to the surface with (near) core–shell-like morphologies visible at intermediate Pt compositions. This segregation is a mechanism for reducing the energetically unfavorable filling of antibonding states of Pt that occurs during alloying with Ru. One may also note that the cohesive energy of HCP Ru is much larger than that of FCC Pt (by ~2.8 eV), whereas the surface energies of typical low-index Miller surfaces of Ru are higher than that of Pt; both of these facts would also point towards the tendency for phase segregation with Pt preferentially occupying surface sites.

This work was published in the Journal of Physical Chemistry A. [6] The DFTB parameter set has also been made freely available to the community (deposited as Supporting Information on the ACS website) and is compatible with the widely used DFTB+ package.

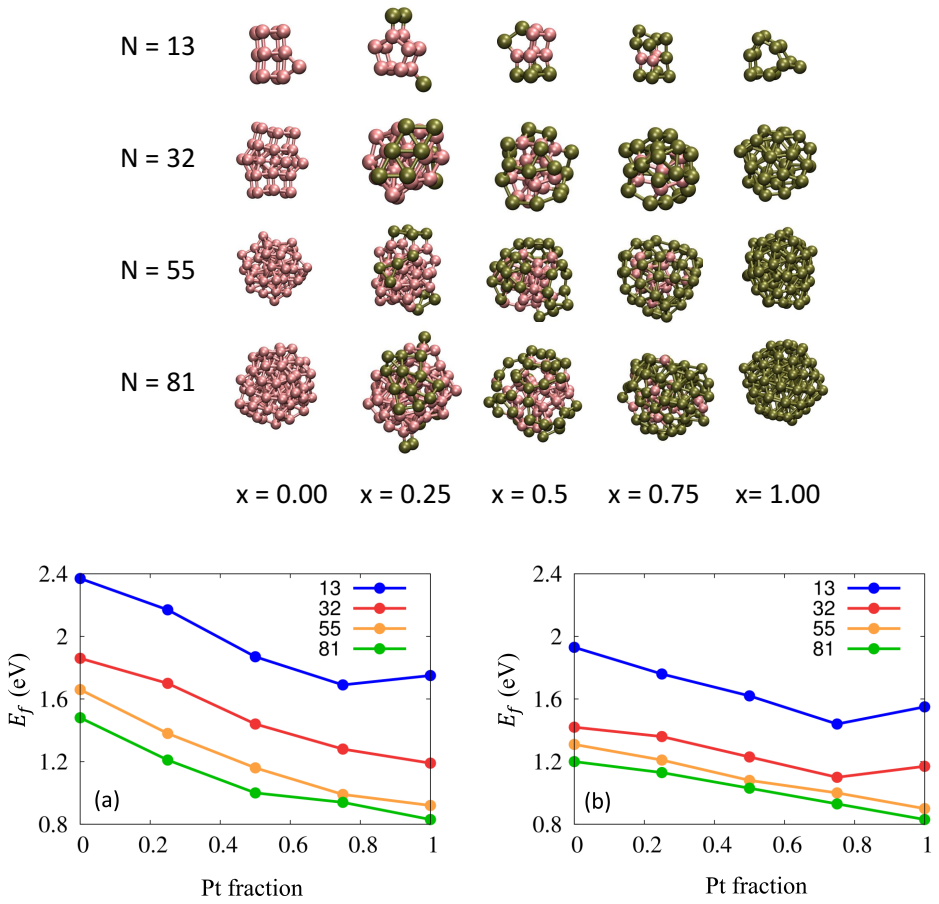

Figure 9: (Top) Morphologies of minimum-energy PtRu clusters of various sizes (N – number of atoms) and compositions (x – Pt fraction) as predicted by our DFTB-based GA implementation. Gold and pink spheres represent Pt and Ru atoms, respectively. (Bottom) Formation energies of GA-optimized PtRu clusters (displayed in upper panel) as a function of Pt concentration, calculated with (left) DFT and (right) DFTB. Cluster sizes (number of atoms) are indicated in the legends.

6. Thermodynamics of Methanol Decomposition on Graphene-Supported Pt_{13} Nanoclusters

Having demonstrated the improved CO tolerance and reduced reaction barriers for CO oxidation on graphene-supported Pt_{13} clusters [1, 4], we turned our attention to the more complex, yet ultimately most relevant, issue of the methanol decomposition reaction (MDR). Using our library of optimized, low-energy Pt_{13} clusters (unsupported and graphene-supported) as model catalysts, we have examined in extensive detail the potential MDR pathways while once again sampling multiple inequivalent binding sites on the cluster surface to generate adequate statistics. While this process is computationally expensive (200-300 DFT structural relaxation calculations), such detailed calculations are essential for extending our understanding of reactions on realistic catalyst surfaces rather than relying on studies performed on idealized crystalline facets.

During the current project period, we were required to revisit our earlier van der Waals DFT calculations of MDR intermediates on Pt clusters due to technical problems that became apparent only upon compilation and analysis of the entire dataset. While vdW corrections are believed to

be important for adsorption studies, we found that existing vdW functionals led to questionable scaling relationships (in addition to causing numerical instabilities in the calculations). We therefore revisited these studies with standard generalized-gradient functionals, which now provide reliable results for the thermodynamics of MDR pathways.

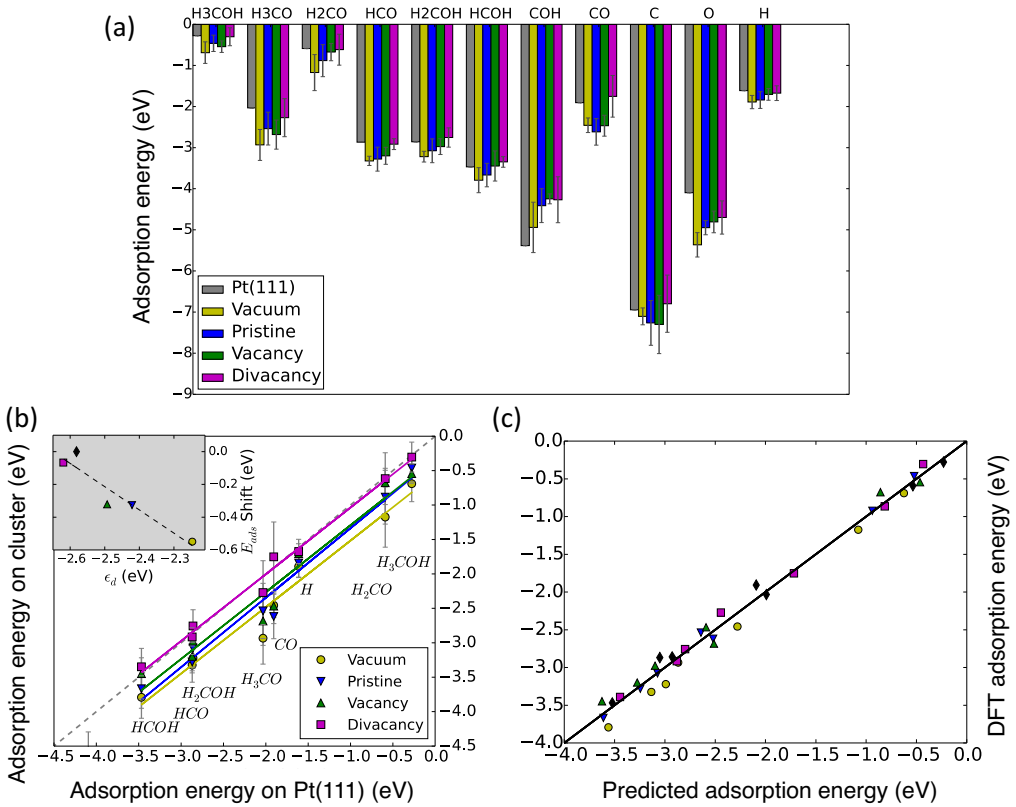

Figure 10: (a) Adsorption energies of MDR intermediates on unsupported and graphene-supported Pt_{13} clusters, as well as Pt(111) surfaces. In general, clusters anchored at support defects bind adsorbates more weakly than unsupported clusters, and can even be competitive with Pt (111) surfaces. Error bars arise from statistical sampling of surface sites. (b) Scaling relation between adsorption energies of MDR intermediates on Pt(111) and Pt_{13} clusters (unsupported and graphene-supported); inset displays the *y*-intercepts of the linear fits, which are inversely correlated with the average *d*–band position of the cluster. (c) Comparison of adsorption energies predicted from scaling relationships with those obtained from DFT calculations.

Figure 10(a) displays the adsorption energies of MDR intermediates on unsupported and graphene-supported Pt_{13} clusters along with baseline calculations for the Pt(111) surface. We find that unsupported clusters bind the reaction intermediates much more strongly than Pt (111) surfaces due to significant undercoordination of surface Pt atoms. The introduction of the graphene support, significantly reduces the binding of adsorbates, with support defects leading to further reduction of the binding energies. The latter effect can be attributed to lowering of cluster *d*-band centers due to strong cluster–support interaction. [1, 4] Indeed, in several cases, binding of MDR intermediates on clusters anchored at divacancy defects is comparable with that on Pt (111) surfaces. This is a *particularly significant result* as it suggests that the simple approach of defect-engineering of an otherwise inert carbon support can appreciably improve the activity of Pt nanoclusters, rendering them competitive with Pt (111), which is one of the best catalysts for MDR.

As ultra-small nanoclusters have no well-defined surface structure (e.g., facets, edges, corners) each surface site is, in principle, distinct from the point of catalytic activity. Nevertheless, it is imperative to seek macroscopic descriptors that can provide insight into the *average* behavior of the surface active sites. Figure 10(b) displays the adsorption energies of MDR intermediates on unsupported as well as graphene-supported Pt_{13} clusters as a function of the adsorption energy on Pt(111) surfaces, from which is immediately apparent that these two adsorption energies are correlated. Furthermore, not only are the adsorption energies on clusters and Pt(111) correlated, but the linear relationship is, to within an excellent approximation, given by a *simple vertical shift* of the dashed parity line in Figure 10(b). In keeping with the trends in Figure 10(a), the unsupported Pt_{13} cluster displays the largest downward shift from the parity due to strongest binding of MDR intermediates; as the binding weakens in going from pristine-graphene-supported clusters to defective-graphene-supported clusters, the linear correlation approaches the Pt(111) parity line. Most interestingly, the vertical offsets of the linear fits are *inversely correlated with the average d-band position* of the Pt_{13} cluster as seen from the inset in Fig. 2 (b). This is *the key finding* of our studies, which is both a new result and of immediate practical relevance for cluster catalysis: in a nutshell, knowing the adsorption energy of an intermediate on Pt(111) and the average *d*-band position of the nanocluster—both trivial calculations within DFT—allows us to obtain from scaling relationships the average adsorption energy of an intermediate on the cluster. Figure 10(c) shows the comparison between predicted adsorption energies from our scaling relationships (fit to a handful of DFT calculations) versus the calculated DFT binding energies for our entire dataset (averaged over multiple surface sites) of MDR intermediates. The data essentially lie exactly along the parity line and confirm the validity of our approach. Thus, we now have for the first time a set of scaling relationships for graphene-supported Pt_{13} nanoclusters, which obviates the need for exhaustive statistical sampling of distinct surface sites. The immediate issues of relevance now are (a) the cluster-size-dependence of these scaling relationships, and (b) their validity for reactions beyond MDR (to the extent that adsorbates bind via similar functional groups). These questions will be examined next. Also, the final step in this study of MDR decomposition is the connection between reaction thermodynamics and kinetics via Brønsted-Evans-Polyani relationships (to enable microkinetic modeling); calculations are underway to uncover these structure–property–function relationships.

The results of this work were published in the Journal of Physical Chemistry C. [7]

7. Kinetics of Methanol Decomposition on Graphene-Supported Pt_{13} Nanoclusters

Subsequent to thermodynamic studies, we focused on understanding the interplay between support defects and the electronic structure of supported nanoclusters, and the consequent impact on the kinetics of the MDR. Using DFT modeling and the nudged-elastic band method, we studied the kinetics of the MDR on defective-graphene supported Pt_{13} nanoparticles, verifying the existence of an initial-state model for prediction of transition state energies on the low-symmetry surface.

The microkinetic model used for this research is based on previous studies of MDR on the Pt(111) surface by Mavrikakis and coworkers. The reaction network being considered encompasses three pathways: the most likely pathway for MDR on Pt(111) single-crystal surface under ultra-high vacuum $H_3COH \rightarrow H_2COH \rightarrow HCOH \rightarrow CO$ (henceforth, Path 1), with the first dehydrogenation step being rate-determining, and two viable but less favorable pathways $H_3COH \rightarrow H_3CO \rightarrow H_2CO \rightarrow HCO \rightarrow CO$ (Path 2) and (ii) $H_3COH \rightarrow H_2COH \rightarrow H_2CO \rightarrow$

HCO → CO (Path 3). Adsorption steps for methanol, carbon monoxide, and hydrogen from the gas phase were also included. The elementary reaction steps are listed in Table 1; reaction step 14 was added to the pathway as it was observed during a transition state calculation on the unsupported Pt_{13} cluster. All MDR intermediates (not methanol, CO, or H_2) are considered to exist only on the Pt(111) surface. The CH_4 production under realistic operating conditions is less than one-tenth the CO production on Pt(111), and is assumed negligible both in this work and others since DFT calculations consistently show C-O bond activation to be very unfavorable over catalysts that are active for the MDR. Complete details of the kinetic model are available in Ref. 8.

Table 1: DFT-sampled barriers for the MDR over the unsupported Pt_{13} nanoparticles and the Pt(111) surface. Pt_{13} results are average values. Steps with no entry had no converged transition state among the sampled reaction steps. No barriers are reported for steps one, six, and seven as these are adsorption/desorption reactions and assumed to have no barrier, as is consistent with the MDR literature. All barriers are in eV.

Step	***Reaction***	***Pt(111)***	***Pt_{13}***
1	$CH_3OH(g) + * \leftrightarrow CH_3OH*$	-	-
2	$CH_3OH* + * \leftrightarrow CH_3O* + H*$	0.47	0.73
3	$CH_3O* + * \leftrightarrow CH_2O* + H*$	0.11	0.22
4	$CH_2O* + * \leftrightarrow HCO* + H*$	0.05	0.65
5	$HCO* + * \leftrightarrow CO* + H*$	0.12	1.19
6	$CO(g) + * \leftrightarrow CO*$	-	-
7	$H_2(g) + 2* \leftrightarrow H* + H*$	-	-
8	$CH_3OH* + * \leftrightarrow CH_2OH* + H*$	0.51	0.62
9	$CH_2OH* + * \leftrightarrow CHOH* + H*$	0.43	1.22
10	$CHOH* + * \leftrightarrow COH* + H*$	0.59	0.58
11	$COH* + * \leftrightarrow CO* + H*$	0.80	0.61
12	$CHOH* + 2* \leftrightarrow CO* + 2H*$	0.24	0.91
13	$CH_2OH* + * \leftrightarrow CH_2O* + H*$	0.29	-
14	$CHOH* + * \leftrightarrow HCO* + H*$	-	1.13

Having a predictor relationship to calculate reaction barriers without requiring numerous DFT transition-state calculations is essential for modeling the MDR on low-symmetry, supported nanoparticles. Therefore, we undertook select MDR reaction barriers calculations on Pt(111) and unsupported Pt_{13} clusters to fit predictor relationships. Even in the case of unsupported Pt_{13} clusters, the fitting of predictor relations for reaction barriers is extremely challenging due to the highly deformable nature of the low-symmetry cluster. Nevertheless, with careful statistical sampling we obtained average DFT-calculated reaction barriers on the unsupported Pt_{13} and the Pt(111) surfaces that are listed in Table 1. The calculated predictor relationship is displayed in Figure 11; interestingly a BEP relationship is not particularly useful for this predictor and an initial-state model proves to be more accurate (as also proposed by Mavrikakis and coworkers). This initial-state predictor model was verified for a few reaction barriers on supported Pt_{13} clusters as well, although accurate statistical sampling of all barriers was not possible due the extreme computational cost (due to the presence of the support).

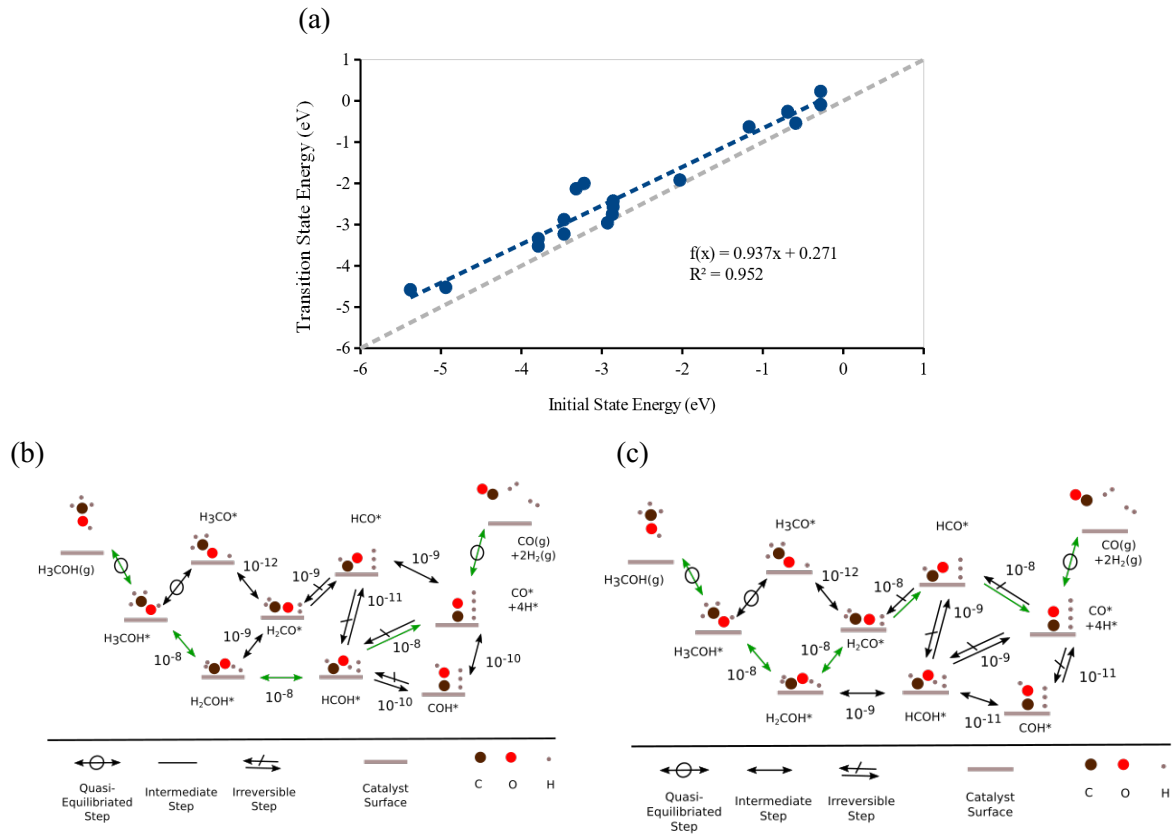

Figure 11: (a) Transition state energies for MDR steps on unsupported Pt_{13} nanoparticles and Pt(111) versus the calculated reaction energies; data points for Pt_{13} results are averages of sampled transition states across different sites; linear regression (blue dashed line) and parity line (gray dashed line) are included. All energies are with respect to the gas-phase reactant of the reaction step. MDR reaction rates over (b) Pt(111) surface and (c) divacancy-graphene supported Pt_{13} catalyst surface. Surface-area-normalized reaction rates are dimensionless and rounded to the nearest power of ten. The most favorable reaction pathway is indicated with green arrows (see legend for details). Hydrogen atoms stacked vertically alongside the intermediates represent those that are adsorbed onto the catalyst surface.

With the initial-state predictor relation at hand, we performed microkineic modeling using an in-house code. We modeled MDR over Pt(111), graphene divacancy-bound Pt_{13}, unsupported Pt_{13} clusters, pristine graphene-supported Pt_{13}, and graphene vacancy-bound Pt_{13}. For the latter three systems, the overall adsorption energies are too strong result in negligible MDR turnover; this is consistent with a different kinetic model in the literature which suggests a nominal turnover frequency for the MDR of $\sim 10^{-15}$ over Pt_4 nanoparticles. Divacancy-graphene supported Pt_{13} are, however, comparable in activity to the Pt(111) slab albeit, via a different active pathway. The reaction rates of the MDR over Pt(111) and over divacancy-graphene supported Pt_{13} are displayed in Figures 11(b, c). For Pt(111), we find the same most-active pathway as reported in the literature – $H_3COH \rightarrow H_2COH \rightarrow HCOH \rightarrow CO$. However, the most active pathway on the divacancy-graphene supported Pt_{13} is $H_3COH \rightarrow H_2COH \rightarrow H_2CO \rightarrow HCO \rightarrow CO$. A significant difference between the MDR network on the two catalysts is that the rate of COH formation is two orders of magnitude lower on divacancy-graphene supported Pt_{13} than on Pt(111), and the irreversible reaction directions favor COH decomposition on the Pt_{13} and COH accumulation on the Pt(111). The result of these differences is that the coverage of COH on

Pt(111) is around 15%-20%, depending on temperature and pressure, whereas the coverage of COH on divacancy-graphene supported Pt_{13} is much lower, around 4%. In short, COH is a secondary catalyst poison on Pt(111) but does not significantly poison the divacancy-graphene supported Pt_{13}; however, the coverage of CO is higher on the divacancy-graphene supported Pt_{13} than on Pt(111), making up for the difference. Finally, a sensitivity analysis shows that the most impactful reaction barrier is the C-H bond breakage to form H_2COH from H_3COH on both divacancy-graphene Pt_{13} system and Pt(111). The sensitivity analysis also shows that the most impactful adsorption energy is for H, as adjusting H adsorption energy affects both the overall reaction equilibrium (thus the thermodynamic driving force) and every single dehydrogenation reaction on the catalyst surface.

8. Structure–Property Relationships of Graphene-Supported PtRu Nanoclusters

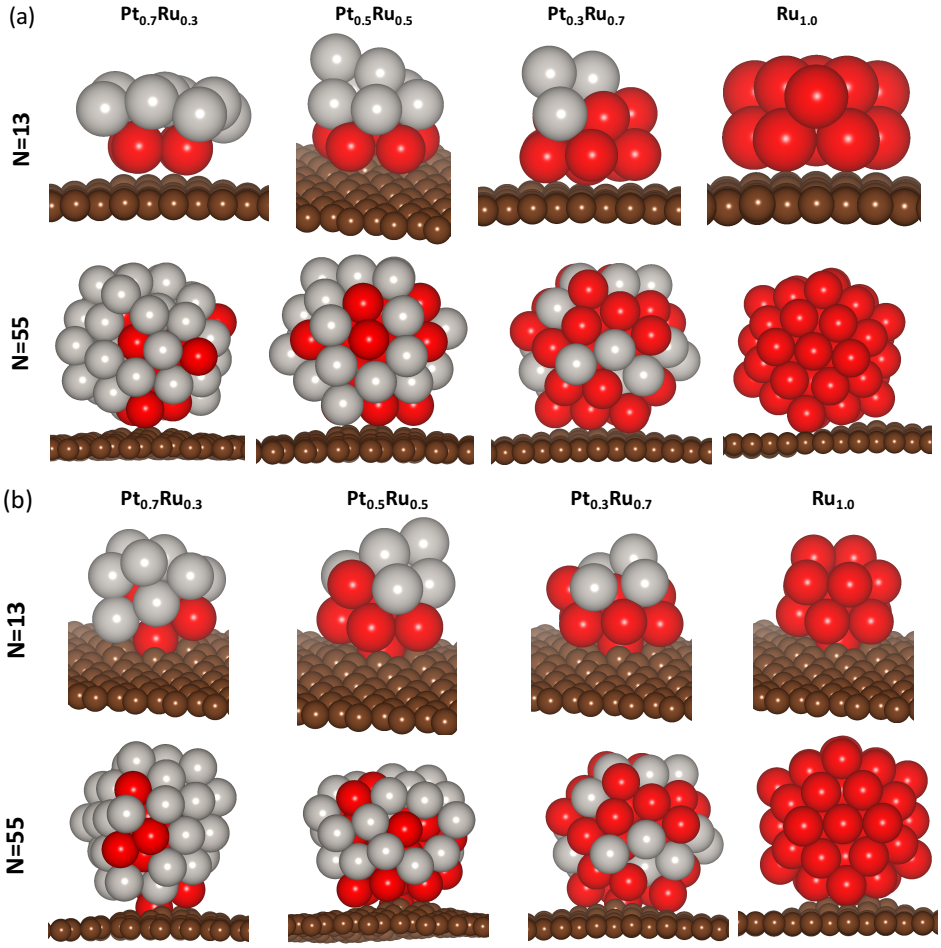

Figure 12: Lowest energy structures for Pt_xRu_{1-x} nanoparticles on (a) pristine graphene supports and (b) supported at a graphene divacancy. Upper and lower rows in each figure are for N=13 and N=55 atom clusters.

We extended our studies of the Pt-Ru alloy system to understand structure-property relationships for graphene-supported nanoclusters. Extending the DFTB parameterization to include C Slater-Koster parameters is challenging not least because there are known problems that arise without inclusion of virtual orbitals; furthermore, even if this parameterization were successful the

computational cost of DFTB-based GAs becomes prohibitive when including support atoms in the calculation. Thus, we attempted to take Tersoff-style Pt-C and Ru-C potentials and parameterize the additional Pt-Ru and Pt-Ru-C interactions based on DFT data. The parameter set is published in Ref. 8. This empirical potential-based GA works seamlessly with our in-house codes that interface with the LAMMPS package (Section 3).

Figure 12 displays the GA-derived and DFT reoptimized lowest-energy structures of Pt_{13} and Pt_{55} nanoclusters on pristine as well as defective (divacancy defect) graphene. Similar to our previous DFTB study, we see that Ru and Pt atoms segregate to the core and shell, respectively. As the Ru-C interaction is stronger than the Pt-C interaction, the particle–support interface is Ru rich. Furthermore, clusters with higher Ru content tend to adopt flatter structures—more "wetting" of graphene—than Pt-rich clusters. While the GA+DFT approach is generally successful in capturing the qualitative structural details of these alloy nanoparticles, there is still a degree of mismatch between the relative ordering of the GA and DFT low-energy structures. Specifically, unlike the Pt-C study (Section 3) wherein the GA optimized structure almost always remained the lowest energy structure after DFT optimization, this is no longer the case here: we need to consider a few low-energy GA structures, reoptimize these with DFT, and then pick the lowest energy candidate for further study. This is not ideal as it requires more work at the computationally expensive DFT level. Thus, it is necessary to develop a better parameter set for the Pt-Ru-C system to allow for more extensive exploration of structure-property relationships.

9. Support Effects in Pt Overlayers on WC

In line with our investigations on the influence of graphene supports on Pt nanoclusters, we also considered an alternative system of Pt overlayers (1-2 monolayers) on WC supports. We employed DFT calculations to study and contrast the suitability of the α and β phases of tungsten carbide (WC) as support (core) materials for Pt shells. We examined the thermodynamic stability of 1-2 layers of Pt on α- and β-WC surfaces, carefully accounting for the delicate balance between epitaxial mismatch strains and chemical bonding between cores and shells, and we also studied the effects of alloying β-WC with Ti to modulate the stability and electronic structure of the core-shell structures (Figure 13). A key finding of our studies is that moderate Ti doping of the metastable β-WC phase significantly improves its stability and, with merely two layers of Pt loading, HER activity comparable or superior to Pt (111) can be attained.

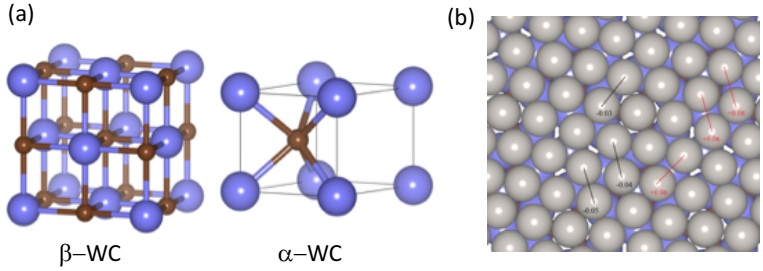

Figure 13: (a) Atomic models of bulk WC phases. (b) Relaxed structure of a Pt ML over α-WC (001) support in the p-(4x4) R15° supercell. Red and black lines indicate regions of tensile and compressive strain, respectively.

The binding energy of hydrogen (HBE) on catalytic surfaces is a widely-accepted descriptor for HER activity in acidic media. The connection between HBEs and the activity of the various WC and Pt/WC surfaces can be made via Sabatier's principle, which is visually rendered by the

so-called "volcano plot". For HER (in acidic media), in particular, the optimal HBE is ~0.37 eV, which is ~0.1 eV more positive than the corresponding value for Pt (111). Figure 14 displays our calculated HBEs, at the most stable surface binding sites, superposed over the volcano plot of from Chen and coworkers who reported the HER activities of various transition metals, transition-metal carbides, and transition-metal-carbide-supported transition metals. While we have yet to calculate exchange currents independently, superimposing our data based on their abscissas (HBEs) over the well-established volcano curve allows us to make some preliminary estimates for our systems. The most significant observation from Figure 14 is that the anticipated exchange current density for Pt_{2ML}/β-$Ti_{0.125}W_{0.875}C$(111) is comparable, if not slightly higher, than that for Pt (111), which is among the best HER catalysts. This is consistent with recent experimental findings from Roman-Leshkov and coworkers who found the HER activity of Pt/β-$Ti_{0.1}W_{0.9}C$ core-shell nanoparticles to be superior to that of Pt (111). On the other hand, we observe that Pt_{ML}/α-WC (001) and Pt_{2ML}/α-WC (001), while towards the upper end of the volcano, are less active than Pt (111), which indicates that *the metastable β-WC phase is more desirable as a support material than the ground-state α-WC phase.* We also find that 12.5% Ti-doping of β-WC yields a more active catalyst than the 22% Ti-doped case as seen from the lower predicted activity when employing the latter as a support.

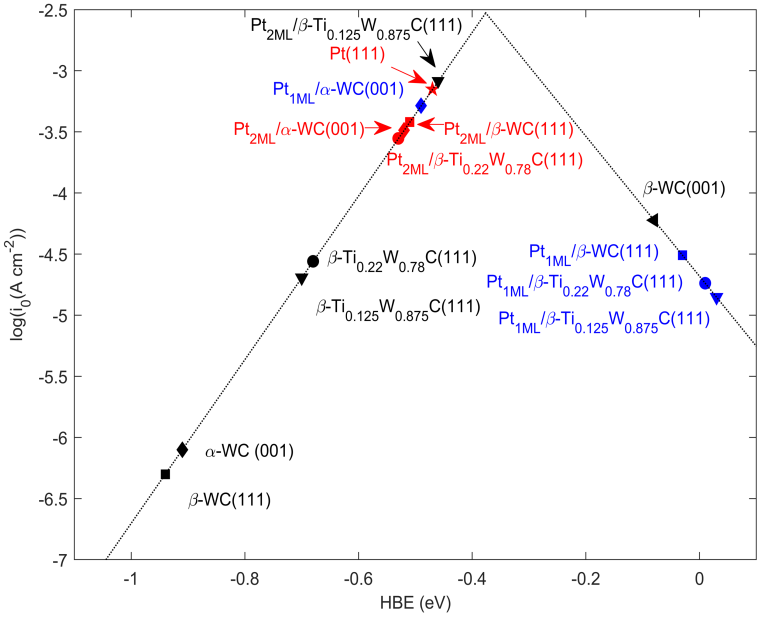

Figure 14. Volcano plot for HER (in acidic media) showing the exchange current densities [log(i_o)] plotted as a function of hydrogen binding energy. The exchange current densities are estimated by superimposing our data for various surfaces, based on their calculated HBEs, over the volcano plot reported by Jingguang Chen's group.

The analysis of catalytic activity thus far has been based on HBEs at the most stable binding sites. There are, of course, variations in HBEs over the Pt layers due to a combination of ligand and strain effects arising from interactions with the support; the distribution of energies become wider on incommensurate and/or rotated surface cells. Focusing on the most promising HER catalysts identified above, namely, Pt_{2ML}/β-$Ti_xW_{1-x}C$ (x=0%, 12.5%, 22%) we performed detailed surface scans of HBEs and found a spread of at most ~0.2 eV for the three Pt_{2ML}/β-$Ti_xW_{1-x}C$ (x=0%, 12.5%, 22%) systems studied. The key point of note here is that our volcano-plot analysis is a conservative one, being based on the largest HBEs, and the inclusion of weaker

binding sites for the $Pt_{2ML}/\beta\text{-}Ti_xW_{1-x}C$ systems will, on average, push the expected values of exchange currents further towards the peak of the volcano.

This work was published in Physical Chemistry Chemical Physics and featured as a *"2018 PCCP HOT Article"*.

10. Support Effects in MoS_2 Overlayers on Au

We performed DFT calculations in support of experiments to study support effects in Au/MoS_2 core-shell nanoparticles. We modeled the Au@MoS_2 nanoparticle as a single layer of MoS_2 (SL-MoS_2) supported on an Au(111) slab, similar to prior studies. To avoid spurious strain effects, we rotated the MoS_2 layer to produce two coincident-site lattices, one with a small biaxial tensile strain (+0.67%) and the second with a moderate tensile strain (+2.48%). These models allow us to explore separately strain and support effects on the activity of the MoS_2 layer.

Figure 15 displays the free energy of hydrogen adsorption (ΔG_H), a descriptor of HER activity in acidic media, for unsupported and Au-supported SL-MoS_2 at standard conditions [300 K and a potential of 0 V vs. Reversible Hydrogen Electrode (RHE)]. In agreement with previous reports, we find that the basal plane of unstrained SL-MoS_2 ML is inert towards HER due to its highly unfavorable ΔG_H ~1.9 eV at a S top-site. At +0.67% and +2.48% strain, the adsorption energy deceases only slightly; the addition of the Au(111) support further lowers ΔG_H by 0.15 and is more significant than the strain effect. The resulting adsorption energies at the S top-sites are still too thermodynamically unfavorable for HER. It is well known that basal plane S-vacancies in MoS_2 are highly active for HER and indeed, we find that ΔG_H drops to ~0.1 eV at a S-vacancy site in unstrained SL-MoS_2. At +0.67% and +2.48% strain, ΔG_H decreases slightly to 0.05 eV and -0.06 eV, respectively, and the addition of the Au support further reduces these adsorption energies to -0.02 eV and -11 eV. Thus, we see once again that support effects are more significant in stabilizing H adsorption than strain effects. Moreover, at low to moderate tensile strains, the support and strain effects act in synergy and render S-vacancy sites more favorable for HER.

This work was published in ACS Applied Energy Materials. [10]

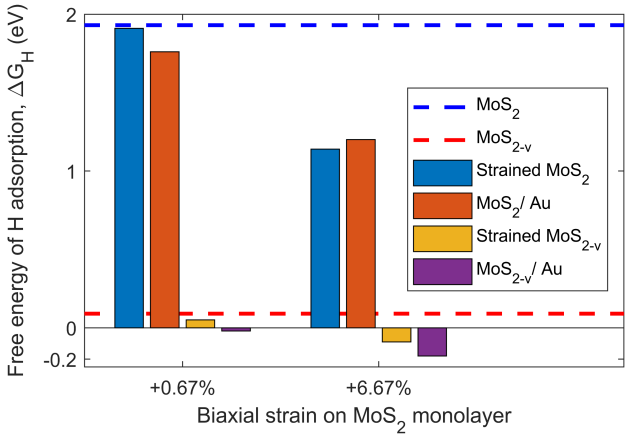

Figure 15. Free energy of H-adsorption (ΔG_H) at S top sites and S-vacancy sites on the basal plane of freestanding SL-MoS_2 and Au(111)-supported SL-MoS_2 MLs at biaxial tensile strains of +0.67% and +2.48%. MoS_2 and $MoS_{2\text{-}v}$ represents the defect free and defective single layers, respectively. Blue and red dashed lines are the reference values of ΔG_H at S top sites and vacancy site, respectively, in the basal plane of unstrained, freestanding SL-MoS_2.

REFERENCES

[1] Fampiou, I.; Ramasubramaniam, A. CO Adsorption on Defective Graphene-Supported Pt_{13} Nanoclusters, *J. Phys. Chem. C* **2013**, 117 (39), 19927-19933.
DOI: https://doi.org/10.1021/jp403468h

[2] Fampiou, I.; Ramasubramaniam, A. Binding of Pt nanoclusters to defects in graphene: adsorption, morphology, and electronic structure, *J. Phys. Chem. C* **2012**, 116 (11), 6543-6555.

[3] Fampiou, I.; Ramasubramaniam, A. Influence of Support Effects on CO Oxidation Kinetics on CO-Saturated Graphene-Supported Pt_{13} Nanoclusters, *J. Phys. Chem. C* 2015, 119, 16, 8703-8710. DOI: https://doi.org/10.1021/acs.jpcc.5b00029

[4] Shi, H.; Auerbach, S.; Ramasubramaniam, A. First-Principles Predictions of Structure-Function Relationships of Graphene-Supported Platinum Nanoclusters, *J. Phys. Chem. C* **2016**, 120 (22), 11899-11909. DOI: https://doi.org/10.1021/acs.jpcc.6b01288

[5] Gasper, R,; Shi, H.; Ramasubramaniam, A. Adsorption of CO on Low-Energy, Low-Symmetry Pt Nanoparticles: Energy Decomposition Analysis and Prediction via Machine-Learning Models, *J. Phys. Chem. C* **2017**, 121 (10), 5612-5619.

[6] Shi, H.; Koskinen, P.; Ramasubramaniam, A. Self-Consistent Charge Density-Functional Tight-Binding Parametrization for Pt–Ru Alloys, *J. Phys. Chem. A* **2017**, 121 (12), 2497-2502.

[7] Gasper, R.; Ramasubramaniam, A. Density Functional Theory Studies of the Methanol Decomposition Reaction on Graphene-Supported Pt_{13} Nanoclusters, J. Phys. Chem. C **2016**, 120 (31), 17408-17417. DOI: https://doi.org/10.1021/acs.jpcc.6b04557

[8] Gasper, R. J. Computational Modeling of the Structure and Catalytic Behavior of Graphene-Supported Pt and PtRu Nanoparticles, Ph.D. Dissertation, University of Massachusetts Amherst, Amherst, MA, 2018.

[9] Jain, A.; Ramasubramaniam, A. Tuning core–shell interactions in tungsten carbide–Pt nanoparticles for the hydrogen evolution reaction, *Phys. Chem. Chem. Phys.* **2018,** *20*, 23262-23271. DOI: 10.1039/C8CP04113J. *Featured as "2018 PCCP HOT Article"*

[10] Bar-Ziv, R.; Ranjan, P.; Lavie, A.; Jain, A.; Garai, S.; Bar Hen, A.; Popovitz-Biro, R.; Tenne, R.; Arenal, R.; Ramasubramaniam, A.; Lajaunie, L.; Bar-Sadan, M. Au-MoS_2 Hybrids as Hydrogen Evolution Electrocatalysts. *ACS Applied Energy Materials* **2019,** *2*, 6043-6050. DOI: 10.1021/acsaem.9b01147